NOZZLE ADMITTANCE FOR HIGHER MODES

R. Kathan, R. Kaess, J. Pieringer, T. Sattelmayer,
Technische Universität München, D-85748 Garching, Germany
Astrium GmbH, Space Transportation TP 25, D-81663 München

Abstract

At the Institute for Thermodynamics (Lehrstuhl für Thermodynamik) at the Technische Universität München nozzle admittances are investigated numerically and experimentally. In particular, nozzle admittances for higher modes are of interest. The knowledge of these is one of the fundamental requirements to compute rocket engine instabilities.

To validate the available numerical results, measurements were undertaken. The presented test facility is operated under cold conditions with pressurized air and consists of a nozzle and a cylindrical chamber. It can be excited at specific frequencies by a siren. The chamber is equipped with sensors in axial and circumferential direction to provide timelines of the pressure.

A method to evaluate the nozzle admittance at the intersection of a combustion chamber and nozzle based on the measurements is presented. The one-dimensional approach considers the homogeneous axial mean flow in the chamber and provides the nozzle admittance for three-dimensional modes. Especially the first transverse modes (T1, T1L1, …) are investigated, because of their important role in the prediction of the stability of rocket engines.

The presented results are compared to numerical computations and the literature.

1. NOMENCLATURE

c	[m/s]	speed of sound
F, G	[m/s]	waves (up- and downstream)
J_m	[-]	Bessel function of the first kind of order m
$k = \frac{\omega}{c}$	[1/m]	wave number
$\dot{m}$	[g/s]	mass flow
m	[-]	number of diametral nodal lines
M	[-]	Mach number
$n-1$	[-]	number of azimutal nodal lines
p'	[Pa]	pressure fluctuation
u'	[m/s]	axial velocity fluctuation
$s = \frac{\omega \cdot r_c}{c}$	[-]	nondimensional frequency
s_{mn}	[-]	the n-th root of $\frac{dJ_m(x)}{dx} = 0$
Y	[m/(s Pa)]	admittance
r_c	[m]	combustion chamber radius
δ	[°]	angle
θ	[°]	azimutal position

2. INTRODUCTION

One of the major challenges in the investigation of rocket engines is the prediction of combustion instabilities. This phenomenon is a result of high pressure fluctuations coupled with unsteady heat release [8]. It can affect the whole rocket by vibrations of the structure and fuel flow interaction to the feed system. The effect can be so tremendous, that the engine could get destroyed by high mechanical stress. This is usually the end of a mission.

Since the frequencies of the pressure fluctuations are conform to the eigenfrequencies of the rocket combustion chamber, the focus is on the identification of the three-

dimensional acoustic wave field inside. The eigenfrequencies strongly depend on the geometry of the combustion chamber and the attached nozzle as well as on fluid flow parameters such as the Mach number, the temperature distribution and the fluid itself.

To identify the influence of the nozzle to the engine, the admittance

$$(1) \quad Y = \frac{u'}{p'}$$

is used. It describes the ratio of the axial velocity fluctuation to the pressure fluctuation. Evaluated at the nozzle entrance it characterizes the acoustic behavior of the nozzle.

The nozzle admittance is typically used as a boundary condition for stability prediction. It strongly depends on the nozzle geometry and the shape of the eigenmode at the nozzle entrance.

Since the admittance of rocket nozzles is affecting the damping of rocket combustion chambers seriously, the knowledge of this value is of major interest. Following Bell [1] a positive value of the real part of the admittance has a stabilizing influence on the rocket engine. Negative values, which can occur at higher modes tend to destabilize it [1], [7]. However, the rocket engine can be stable even if the admittance is negative due to convective transport through the nozzle.

In this investigation the focus is on the acoustic behavior. Pieringer [7] provides values for the admittance simulated with a 3D tool that were compared against the numerically investigated 1D theory given by Bell [1]. The presented experiments will validate their results.

Pressure data are provided at some specific positions along a cylindrical combustion chamber. With a simple modal decomposition and a proper extension of a one-dimensional acoustic wave propagation approach, the wave field inside the chamber can be computed as well as the admittance.

3. HIGHER MODES IN ROCKET COMBUSTION CHAMBERS

3.1. Definitions

The notation of the eigenmodes in rocket combustion chambers is often based on the nomenclature of a cylinder with solid walls. This is useful for rough estimations, but not for profound investigations.

Especially for transverse modes the differences of the mode shapes in cylinders compared to rocket combustion chambers are tremendous. Since the downstream end of a cylindrical rocket combustion chamber is connected to a nozzle, the analogy to the cylinder solution and its boundary is insufficient for the modeling.

For example, pure transverse modes (T1, T2,…) can occur in a cylinder while they cannot occur in a rocket combustion chamber with an attached nozzle as shown in FIGURE 1. The reason is that the downstream boundary condition which is different from a solid wall has to be satisfied. As a consequence the pressure gradient in axial direction must be considered.

Instead of applying the cylinder nomenclature to rocket engines, it is more appropriate to define mode classes as shown in FIGURE 2. m indicates the mode class with respect to transverse modes only. For example, mode class 0 ($m=0$) contains modes with no angular dependence such as longitudinal modes L1, L2, …. Mode class 1 consists of modes with a first transverse characteristic in azimutal direction (T1L1, T1L2, T1L3, …). Every mode class starts at its cut-on frequency $s_{cut-on,mn}$. Below the cut-on frequency a mode class cannot exist. Radial modes are not taken into account since their cut-on frequencies are above the considered frequency range. Subsequently, we use the term higher modes for mode classes above 0.

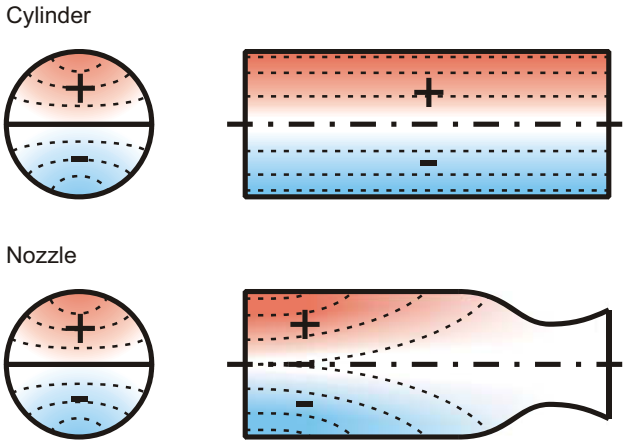

FIGURE 1. T1 mode in a cylinder compared to a similar mode in a rocket combustion chamber with an attached nozzle

The cut-on frequency depends on the Mach number and is given e. g. by Bell [1] as

$$(2) \quad s_{cut-on,mn} = s_{mn} \cdot \sqrt{1 - M^2}$$

The focus of this investigation lies on the admittance of mode class 0 and 1, below the cut-on frequency of mode class 2 and the radial modes. Therefore, the modes above are not taken into account in the presented study. An overview of some mode classes and their corresponding values such as the cut-on frequency are given in TAB 1.

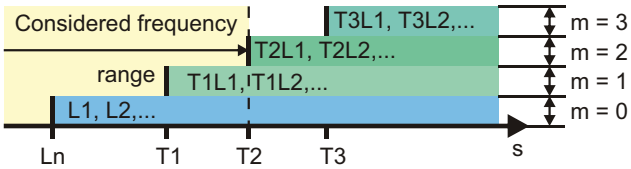

FIGURE 2. Schematic overview of different mode classes and the considered frequency range.

Mode class m	n	Characteristic	s_{mn}	$s_{cut-on,mn}$ for $M=0,25$
0	1	L (L1, L2, …)	0	0
1	1	T1 (T1L1, …)	1,8412	1,7827
2	1	T2 (T2L1, …)	3,0542	2,9572
3	1	T3 (T3L1, …)	4,2013	4,0689

TAB 1. Different mode classes and values for the corresponding cut-on frequencies.

3.2. Modal decomposition

Due to the fact that rocket combustion chambers are usually cylindrical, a cylindrical coordinate system is chosen.

The pressure and the axial velocity inside the rocket engine can be written as the sum of a mean and a fluctuation value:

$$(3)\quad \begin{aligned} p &= p_0 + p' \\ u &= u_0 + u' \end{aligned}$$

Mean values are denoted with the index 0 and fluctuating values are indicated with ‘. In the following we only consider harmonic pressure fluctuations at one specific frequency ω.

$$(4)\quad p'(x,r,\theta,t) \hat{=} \mathrm{Re}\left(\hat{p}(x,r,\theta,\omega)\cdot e^{i\omega t}\right)$$

The complex amplitude can be written as an infinite sum of modes [7]

$$(5)\quad \hat{p}(x,r,\theta.\omega) = \sum_{m=0}^{\infty}\sum_{n=1}^{\infty} \hat{p}^{mn}(x,r,\theta,\omega)$$

Each of these modes can be split into

$$(6)\quad \hat{p}^{mn}(x,r,\theta,\omega) = \rho\cdot c\cdot P^{mn}(x,\omega)\cdot R^{mn}(r) \cdot\Theta^{mn}(\theta)$$

with a weighting function for each direction. $P^{mn}(x,\omega)$ represents the axial, $R^{mn}(r)$ the radial and $\Theta^{mn}(\theta)$ the transverse direction. When considering only standing waves, the solutions for a non-rotating mode in a cylindrical volume in radial and transverse directions become:

$$(7)\quad R^{mn}(r) = J_m\left(s_{mn}\frac{r}{r_c}\right)$$

$$(8)\quad \Theta^{mn}(\theta) = \cos\left(m\cdot\left(\theta+\delta^{mn}\right)\right)$$

m in Equation (7) and (8) is equal to the number of the mode class (e. g. $m = 1$ for mode class 1) and $n-1$ describes the number of azimutal nodal lines.

In the axial direction the influence of the mean flow has to be considered. The solution

$$(9)\quad P^{mn}(x,\omega) = F^{mn}\cdot e^{-i\cdot k_{x+}^{mn}\cdot x} + G^{m}\cdot e^{-i\cdot k_{x-}^{mn}\cdot x}$$

can be found by solving the wave equation [1].

Since only mode class 0 and mode class 1 occur in the investigated frequency range as shown in FIGURE 2, other mode classes are not taken into account. The values for m and n can be found in TAB 1. While n is always equal to 1, EQUATION (5) can be reduced to

$$(10)\quad \hat{p}(x,r,\theta.\omega) = \sum_{m=0}^{\infty}\hat{p}^{m}(x,r,\theta,\omega)$$

The solutions for the complex pressure amplitude of mode class 0 and mode class 1 are

$$(11)\quad \hat{p}^{0}(x,\theta,r_c) = \rho\cdot c\cdot\left(F^{01}\cdot e^{-i\cdot k_{x+}^{01}\cdot x} + G^{01}\cdot e^{-i\cdot k_{x-}^{01}\cdot x}\right) \cdot J_0(s_{01})$$

$$(12)\quad \hat{p}^{1}(x,\theta,r_c) = \rho\cdot c\cdot\left(F^{11}\cdot e^{-i\cdot k_{x+}^{11}\cdot x} + G^{11}\cdot e^{-i\cdot k_{x-}^{11}\cdot x}\right) \cdot J_1(s_{11})\cdot\cos\left(\theta+\delta^{11}\right)$$

with the wave number

$$(13)\quad k_{x\pm}^{01,11} = \frac{k}{1-M^2}\cdot\left(-M\pm\sqrt{1-\left(\frac{k_y^{01,11}}{k}\right)^2\cdot\left(1-M^2\right)}\right)$$

in axial direction including the azimutal wave number

$$(14)\quad k_y^{01,11} = \frac{s_{mn}}{r_c}$$

(11) is the complex pressure amplitude of mode class 0 and (12) the one of mode class 1. For the calculation of the pressure field inside the cylinder the four complex values $F^{01}, G^{01}, F^{11}, G^{11}$ and the real value δ^{11} have to be found. δ^{11} is a correction angle for mode class 1 that considers the position of the pressure node in azimutal direction.

Finally the axial velocity fluctuations are obtained

$$(15)\quad \hat{u}^{0}(x,\theta,r_c) = \left(\kappa_+^{01}\cdot F^{01}\cdot e^{-i\cdot k_{x+}^{01}\cdot x} + \kappa_-^{01}\cdot G^{01}\cdot e^{-i\cdot k_{x-}^{01}\cdot x}\right) \cdot J_0(s_{01})$$

$$(16)\quad \hat{u}^{1}(x,\theta,r_c) = \left(\kappa_+^{11}\cdot F^{11}\cdot e^{-i\cdot k_{x+}^{11}\cdot x} + \kappa_-^{11}\cdot G^{11}\cdot e^{-i\cdot k_{x-}^{11}\cdot x}\right) \cdot J_1(s_{11})\cdot\cos\left(\theta+\delta^{11}\right)$$

with

$$(17)\quad \kappa_{\pm}^{01,11} = \frac{k_{x\pm}^{01,11}}{k - M\cdot k_{x\pm}^{01,11}}$$

$\kappa_{\pm}^{01,11}$ represents a correction factor to achieve the axial velocity component. It is computed by the ratio of the principal wave number to the axial wave number considering the Mach number.

3.3. Validation with simulated data

Since each dynamic pressure sensor provides one complex value (pressure amplitude and phase), at least five sensors are necessary to solve the system of linear equations

$$(18)\quad \hat{p}_i(x_i,\theta_i,r_c)-\left(\hat{p}^0(x_i,\theta_i,r_c)+\hat{p}^1(x_i,\theta_i,r_c)\right)\rightarrow \min$$

where $\hat{p}_i(x_i,\theta_i,r_c)$ is the measured pressure provided by the sensor i. A nonlinear Levenberg-Marquardt algorithm was used to minimize the deviation between the theoretical solution and computed data.

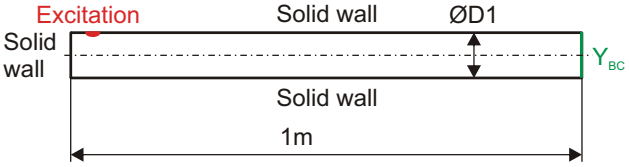

FIGURE 3. Computational domain with the boundary conditions.

To validate the described method a test case with COMSOL (acoustic solver, no mean flow, 3D) was set up to provide simulated data. FIGURE 3 shows the computational domain which consists of a cylinder with the diameter equal to the experiment. The boundary condition on one side was a solid wall, on the other side the admittance was set to a certain value.

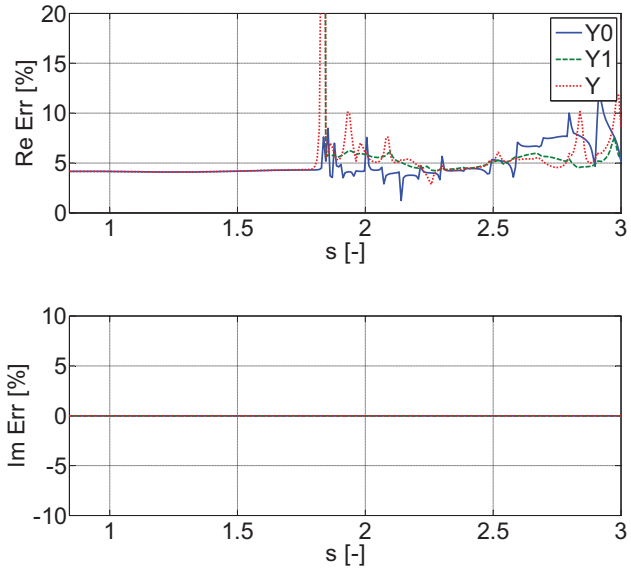

FIGURE 4. Comparison of the admittance set for the boundary condition and the recalculated values for different mode classes. Y is the complete admittance considering both modes simultaneously. The imaginary part is zero for all frequencies.

The excitation was provided by an adequate boundary condition in radial direction. The calculated admittance was compared to the specified admittance that was used for the boundary condition. The error for each mode class plotted in FIGURE 4 that is defined as

$$(19)\quad Err=\frac{Y-Y_{BC}}{Y_{BC}}$$

shows differences of about 4% for the real part of the value with higher errors at some frequencies. Since the admittance is defined as the ratio of the velocity to the pressure fluctuations, the error can increase for low quantities of the pressure fluctuation and limited computer accuracy. The imaginary part is almost identical with the given admittance for all frequencies.

4. EXPERIMENTAL SETUP

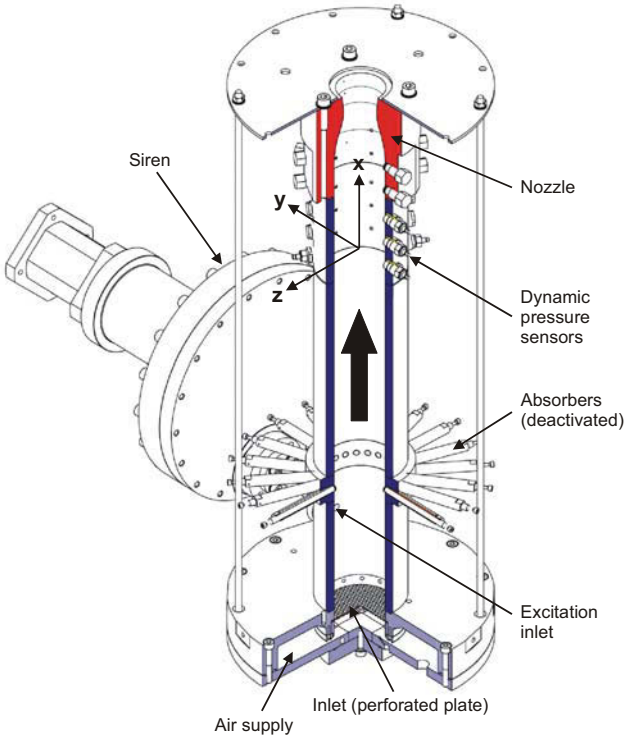

FIGURE 5. Test facility and its main components. The black arrow indicates the flow direction.

The experiment consists of a cylindrical part (combustion chamber) and a nozzle. Instead of an injector faceplate that is usually attached to rocket combustion chambers, a perforated plate is used. The experiment is operated with pressurized air but without combustion. The air is provided by a high pressure feed system with several mass flow control units.
An overview of the test facility is given in FIGURE 5. It consists of the following parts:

1) Combustion chamber and nozzle with an absorber ring (deactivated).
2) Excitation
3) Supply system
4) Measurement technique

4.1. Combustion chamber and nozzle

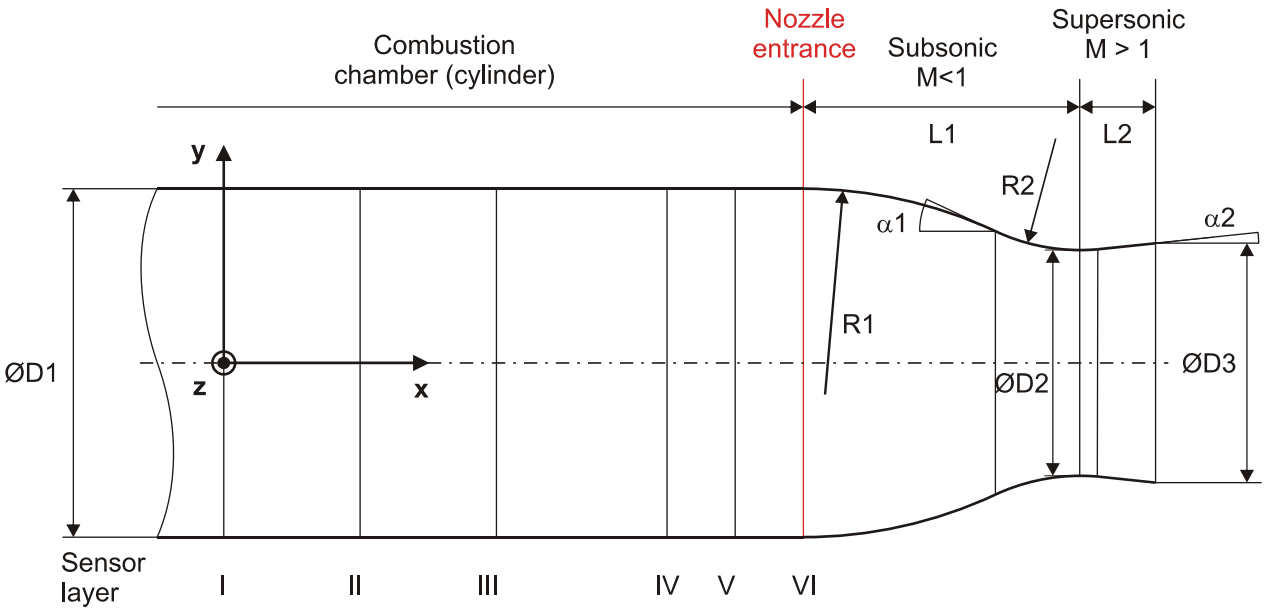

FIGURE 6. Nozzle geometry and sensor layers

The geometry of the nozzle has been selected such that it is fully specified using the few geometry parameters of the nozzle available in the admittance calculation code developed by Bell [1]. Those parameters are the diameter of the combustion chamber, the two radii of the curvature of the nozzle, the nozzle angle in the subsonic part and the length of the subsonic nozzle part. The geometry is shown in FIGURE 6 with the appropriate values provided in TAB 2.

The nozzles consist of a subsonic and a supersonic part to make sure that the flow is accelerated through the nozzle throat from subsonic to supersonic velocities and that always sonic conditions are provided in the nozzle throat.

Symbol	Value	Unit
ØD1	92	mm
ØD2	60	mm
ØD3	64	mm
R1	~119	mm
R2	~53	mm
L1	107	mm
L2	73	mm
L3	25	mm
α1	25	°
α2	6	°

TAB 2. Nozzle dimensions

4.2. Excitation

An external siren is used to excite the chamber at specific frequencies. The inlet is connected in radial direction to the combustion chamber 580 mm upstream from the nozzle entrance. The siren disc shown in FIGURE 7 provides 56 pulses per revolution and is driven by an electric motor which allows a maximum excitation frequency of 5600 Hz ($s \sim 4,75$).

The shape of the siren outlet (not shown) is adapted such that it provides almost perfect smooth sinusoidal pulses.

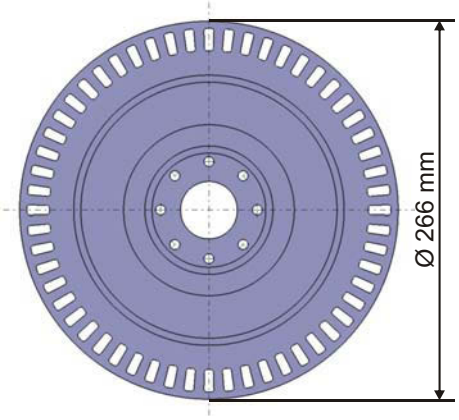

FIGURE 7. Siren disc with 56 holes

4.3. Supply system

The air supply is provided by two different control units, one for the main air mass flow and one for the siren excitation.

The main air mass flow of 1100 g/s enters the combustion chamber through the inlet (perforated plate). The siren air mass flow was 50 g/s at a pressure of ~ 7,3 bar. The total mass flow through the combustion chamber was 1150 g/s and the static pressure was 1,65 bar. The Mach number in the combustion chamber was:

(20) $$M = \frac{\dot{m}}{\rho \cdot c \cdot r_c^{\,2} \cdot \pi} = 0{,}25$$

The speed of sound was calculated to $c=334m/s$ considering that the temperature inside the combustion chamber was approximately 5°C in the tests.

Considering the Mach number, the cut-on frequencies are presented in TAB 1.

4.4. Measurement technique

The combustion chamber is equipped with ports in flow as well as in circumferential direction (FIGURE 6 and TAB 3). The pressure measurements are performed with piezoelectric sensors (PCB Piezotronics, type M106B) connected to an A/D data acquisition unit (National Instruments NI PXI-4472). This type of pressure transducer is internally protected against mechanical vibrations and uses a high pass filter to suppress the mean pressure.

Sensor layer	x [mm]	θ [°]
I	0	0, 60, 120, 180, 240, 300
II	36	0, 60, 120, 180, 240, 300
III	72	0, 60, 120, 180, 240, 300
IV	117	0, 60, 120, 180, 240, 300
V	135	150, 270
VI	153	0, 60, 120, 180, 240, 300

TAB 3. Sensor positions

The analog signals were simultaneously sampled at 2^{15} Hz for one second of measurement time. Afterwards, they were Fourier transformed. The amplitude and phase of the acoustic pressure corresponding to the excitation frequency were extracted from the frequency spectrum.

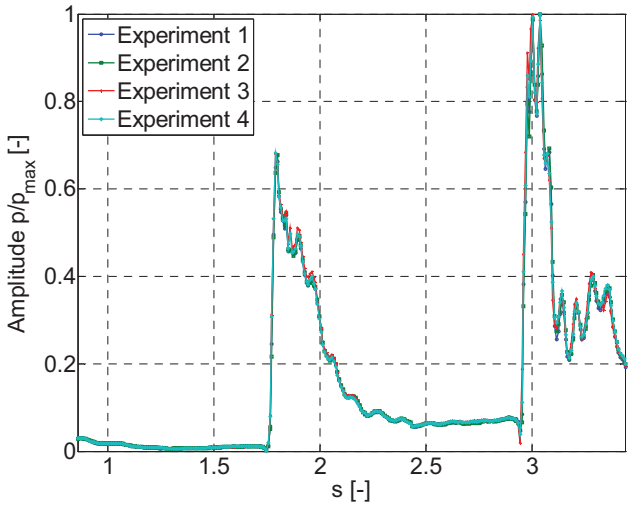

FIGURE 8. Pressure amplitude of the reference pressure sensor normalized with its maximum for each experiment.

For each excitation frequency several recordings were acquired to obtain a representative time average of the acoustic pressure in terms of amplitude and phase.

Ten sensors were used in this investigation. To increase the number of pressure data, the experiment was run four times with the sensors at different positions (one sensor was left at its original position and used as a reference). The reproducibility of the experiment was checked by plotting the normalized variation of the pressure measured by the reference sensor as shown in FIGURE 8. Excellent results were obtained.

5. AVAILABLE DATA

The experimental results are compared to two available sets of data that were validated against each other by Pieringer [7].

The available data are:

1) Simulated results by Pieringer [7]
2) Numerical solution provided by Bell and Zinn [1], [2]

5.1. Simulated results

The admittance of the nozzle was computed with the 3D simulation tool PIANO [7] based on the Acoustic Perturbation Equations (APE) [4], [5], [6], [8]. The results showed a nearly constant admittance over the nozzle entrance plane which is required for the presented experimental approach.

The available values are for the admittance close to the cut-on frequency of mode class 1.

5.2. Theoretical solution

Bell and Zinn [1], [2] provide experimental results in comparison to the theory developed by Crocco [3] for the admittances of choked nozzles that considers three-dimensional flow oscillations including higher modes. By specifying the mode class this method provides the corresponding admittance and was in good agreement to the experimental data.

6. RESULTS

The measurements discussed in this section have been performed for a frequency range from 1.000 Hz to 4.000 Hz with a 10 Hz step size ($s \sim 0{,}86..3{,}44$). Below the cut-on frequency for mode class 1, mode class 0 was excited for its own. Above, mode class 1 was excited simultaneously with mode class 0.

First the quality of the reconstructed values is analyzed. FIGURE 9 and FIGURE 10 show the pressure measured by two sensors (out of 32, given in TAB 3) at different positions compared to the reconstructed values following EQUATION (5). They are in nearly perfect agreement with each other. At some frequencies minor differences in the phase occur which are irrelevant due to very low amplitudes of the pressure.

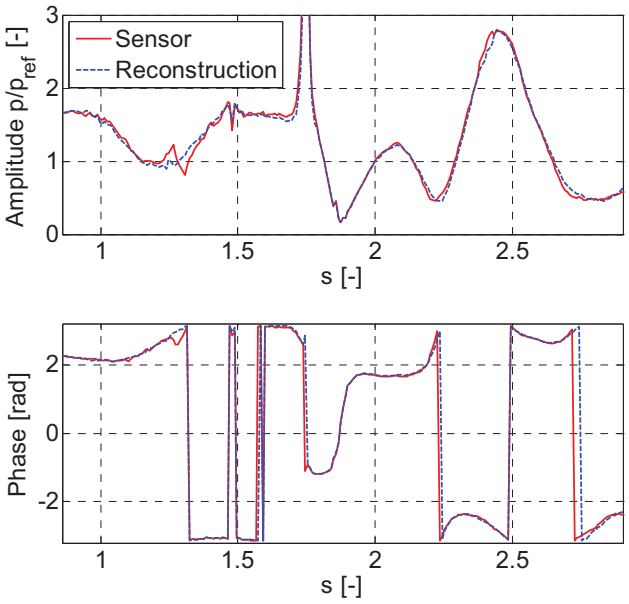

FIGURE 9. Measured and reconstructed amplitude and phase of a sensor at x = 36 mm, $\theta = 180°$

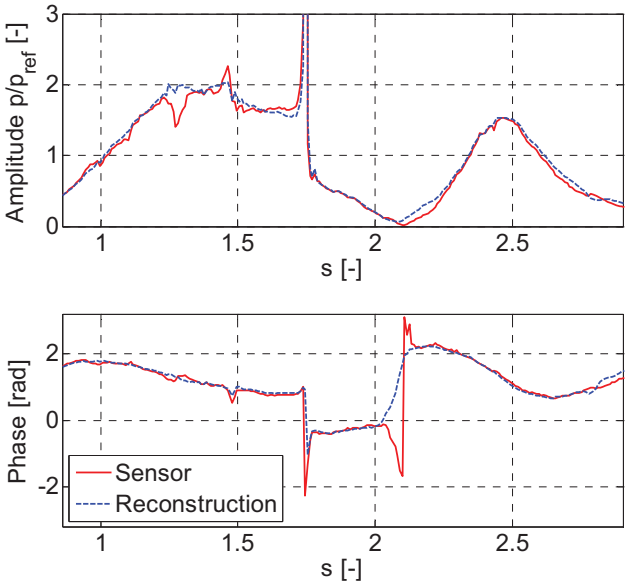

FIGURE 10. Measured and reconstructed amplitude and phase of a sensor at x = 117 mm, $\theta = 240°$

6.1. Excitation below the cut on frequency for mode class 1

The theory and the experimental data for the nozzle admittance are in very good agreement to each other, as shown in FIGURE 11. Especially for low frequencies the real part fits almost perfectly. For the imaginary part the experiment is in good agreement with the theory. At frequencies above $s \sim 1{,}00$ small deviations occur, which is similar to the investigations by Bell and Zinn [1], [2].

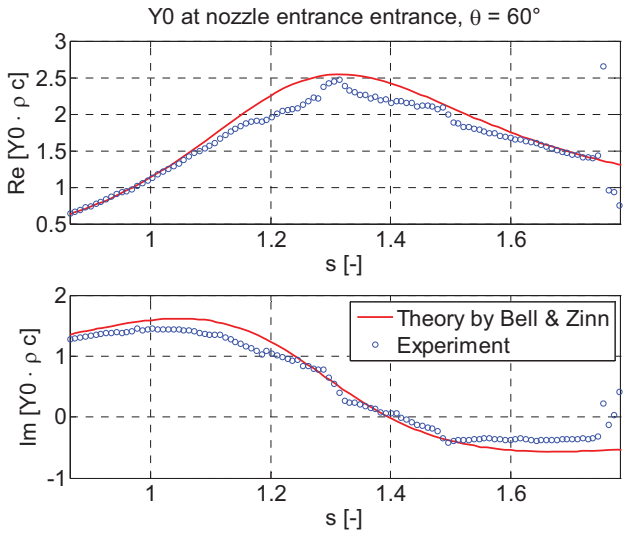

FIGURE 11. Results for mode class 0

At frequencies close to the cut-on frequency of mode class 1 (given in TAB 1), some deviations can be recognized. They are based on low accuracy of the very small pressure values at these frequencies.

In summary, the results delivered by the simulation and the theory were experimentally confirmed for mode class 0.

6.2. Excitation above the cut-on frequency for mode class 1

The results for mode class 1 shown in FIGURE 12 are also in very good agreement to the theory. For frequencies close to the cut-on frequency for mode class 1 (given in TAB 1), the experiment shows minor deviations from the theoretical values caused by small pressure values. At higher frequencies of about $s \sim 2{,}4$, the experimental data are above the theoretical values.

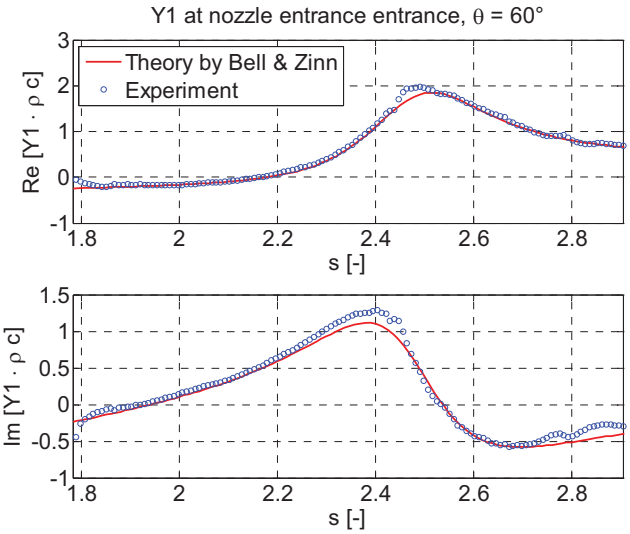

FIGURE 12. Results for mode class 1

TAB 4 shows the experimental results at one particular frequency. These are compared to the theory and the

simulated results and are in very good accordance with each other.

	Real part of Y1 at $s = 1{,}84$	**Imaginary part of Y1 at** $s = 1{,}84$
Theory	-0,22	-0,13
Simulation, $r = r_c$	-0,20	-0,10
Simulation, $r = 0{,}5 \cdot r_c$	-0,19	-0,11
Experiment	-0,21	-0,09

TAB 4. Comparison of the admittance for mode class 1 at one specific frequency

7. CONCLUSION

The real and imaginary parts of the admittance are in very good agreement with the theoretical values. For both investigated mode classes, it can be easily seen, that the values of the real and imaginary part of the admittance are equal to the theoretical values for almost every frequency. At some frequencies minor differences occur.

For mode class 0 the absolute values of the real and the imaginary part of the experimental results are marginally below the theory for the whole frequency range. This yields in lower damping.

For mode class 1 it can be concluded, that the simulated values and the theory can be confirmed. The experiment delivers the same negative real part of the nozzle admittance for specific frequencies which corresponds to a destabilizing effect.

8. OUTLOOK

In future investigations the modal decompositions will be extended to consider mode class 2 to provide nozzle admittances for this mode class as well.

9. ACKNOWLEDGEMENTS

This project was supported by Astrium GmbH, Space Transportation and Prof. Dr.-Ing. Jan Delfs from the Institute of Aerodynamics and Flow Technology at the German Aerospace Research Center who provided PIANO.

Their support is gratefully acknowledged.

10. REFERENCES

[1] Bell, W. A.: Experimental determination of three-dimensional liquid rocket nozzle admittances, Georgia Institute of Technology Atlanta, Dissertation, 1972

[2] Bell, W. A., Zinn, B. T.: The prediction of three-dimensional liquid-propellant rocket nozzle admittances, Georgia Institute of Technology Atlanta, NASA CR-121129

[3] Crocco, L., Sirignano, W. A.: Behaviour of supercritical nozzles under three-dimensional oscillatory conditions / North Atlantic Treaty Organisation, 1967 (AGARDograph 117)

[4] Ewert, R., Meinke, M., Schröder, W.: Computation of sound radiation from a trailing edge applying acoustic perturbation equations, 3rd swing aeroacoustics workshop, Stuttgart, Germany, 2002 – Aerodynamisches Institut, RWTH Aachen

[5] Ewert, R., Meinke, M., Schröder, W.: Computation of trailing edge noise via LES and acoustic perturbation equations, 8th AIAA/CEAS aeroacoustics conference and exhibit, Breckenridge, Colorado, 2002

[6] Ewert, R., Meinke, M., Schröder, W.: Acoustic perturbation equations based on flow decomposition via source filtering, Journal of computational physics 188 (2003), P. 365-398

[7] Pieringer, J.: Simulation selbsterregter Verbrennungsschwingungen in Raketenschubkammern im Zeitbereich, Dissertation, Technische Universität München, 2008

[8] Pieringer, J., Sattelmayer, T., Fassl F.: Simulation of Combustion Instabilities in Liquid rocket Engines with Acoustic Perturbation Equations, Journal of Propulsion and Power, Vol. 25, No. 5, September-October 2009